

Materials growth for manufacturable InAs high electron mobility transistors and circuits

Brian R. Bennett^{a)}, Brad P. Tinkham, and J. Brad Boos
Naval Research Laboratory
Washington, DC
Michael D. Lange and Roger Tsai
Northrop Grumman Space Technology, Inc.
Redondo Beach, CA

*For submission to JVST-B
9/26/03 12:52 PM*

Abstract

High electron mobility transistors (HEMTs) with InAs channels and antimonide barriers were grown by molecular beam epitaxy. Both Si and Te were successfully employed as n-type dopants. Sheet resistances of 90-150 Ω/\square were routinely achieved on a variety of heterostructures with uniformities as low as 1.5% across a 75 mm wafer. X-ray diffraction measurements show that the InAs channels are in tension, coherently strained to the Al(Ga)Sb buffer layers. Atomic force microscopy measurements demonstrate that the surfaces are relatively smooth, with rms roughness of 8-26 Å over a 5 x 5 μm^2 area. These results demonstrate that the growth of InAs HEMTs has progressed to the point that the manufacture of circuits should be feasible.

^{a)} email: brian.bennett@nrl.navy.mil

I. INTRODUCTION

The first high electron mobility transistors (HEMTs) were fabricated with GaAs channels and AlGaAs barriers. In order to achieve higher electron velocity (translating to higher frequency operation), In was added to the channel. Typical structures have $\text{In}_{0.2}\text{Ga}_{0.8}\text{As}$ channels that are *pseudomorphically* strained to the GaAs lattice constant (PHEMTs). In order to improve performance further, additional In was added to the channel and the barrier material was changed to InAlAs; the larger lattice constants were accommodated by using InP substrates. The logical progression of this trend is to use pure InAs as the channel. Arsenides are not suitable barriers but antimonides such as AlSb and AlGaSb are. Advantages of this material system include the high electron mobility ($30,000 \text{ cm}^2/\text{V}\cdot\text{s}$ at 300K) and velocity ($4 \times 10^7 \text{ cm/s}$) of InAs,¹ and a large conduction band offset between InAs and AlSb (1.35 eV). A few groups began to explore InAs HEMTs over a decade ago.^{2,3,4,5,6} To date, most research has focused on demonstrating discrete devices. The results have been promising. For example, we have achieved HEMT characteristics with a unity-current-gain cut-off frequency, f_T , of 250 GHz for a $0.1 \text{ }\mu\text{m}$ gate length.⁷ The low-power potential for this technology is demonstrated by f_T values of 90 GHz at a bias of only 100 mV.⁸ Substantially higher voltages (and hence higher operating powers) are required for InP- or GaAs-based devices. Recently, values of f_{max} , the maximum frequency of oscillation, exceeding 100 GHz have been reported for InAs HEMTs.^{9,10,11} In this work, we focus on making the growth and fabrication process more robust with the goal of enabling production of circuits based upon InAs HEMTs. The work described here led to the recent

demonstration of microwave monolithic integrated circuit (MMIC) low-noise amplifiers based upon InAs HEMTs.¹¹

II. EXPERIMENTAL

Samples were grown by solid-source molecular beam epitaxy (MBE) on Riber 32P and 21T systems. The 32P is a horizontal system and can accommodate a single substrate 50 mm in diameter; the 21T is a vertical system and can accommodate a single substrate 75 mm in diameter. Growth temperatures were measured by transmission thermometry.¹² The heterostructure cross-section and band diagram for one of our baseline growths on the 21T is shown in Fig. 1. We will describe the growth process for this sample (A) in detail. Later, we will discuss variations in the heterostructure and growth parameters.

The oxide is removed from the semi-insulating GaAs (100) substrate by heating the sample to 630°C under an As₂ flux. A 2000 Å buffer layer of GaAs is then grown at 600°C. After growth of GaAs, the substrate temperature is lowered to 540°C for growth of a 1.7 μm buffer layer of AlSb to accommodate the 8% lattice mismatch. Then, an additional 3000 Å of Al_{0.70}Ga_{0.30}Sb is grown at 540°C. After the AlGaSb, the substrate temperature is lowered to 510°C for the growth of a 500 Å AlSb barrier. This is followed by a 150 Å InAs channel. During the channel growth, the substrate thermocouple temperature is ramped down by 40°C to compensate for the sample heating caused by additional absorption of heater radiation by the narrow-band-gap InAs.¹² As a result, the sample temperature measured by transmission thermometry remains at 510 ± 10°C. The channel is followed by a 75 Å AlSb barrier/spacer, a 60 Å AlSb(Te) donor layer, 50 Å AlSb and 40 Å InAlAs barriers, and a 20 Å InAs cap, all grown at 510°C. The Te doping

was supplied by a GaTe source at 550°C.¹³ The growth rate was 1.0 monolayers (ML)/s for the GaAs, AlSb, and AlGaSb buffer layers as well as the InAlAs barrier. The AlSb barriers were grown at 0.6 ML/s. The InAs channel and cap were grown at 0.4 ML/s. Arsenic was supplied by a Riber valved cracker, with the tip temperature at 950°C to produce As₂. Antimony was supplied by an Applied Epi valved cracker, with the tip temperature at 900°C to produce Sb₂ (and possibly Sb₁). The As valve is closed during all antimonide layers to minimize As incorporation. Migration-enhanced epitaxy is used at interfaces between InAs and AlSb to achieve InSb-like bonds.^{14,15} Growth rates were calibrated by reflection high-energy electron diffraction (RHEED) oscillations. Cation growth rates were determined by conventional RHEED oscillations with an anion:cation flux ratio greater than unity. Anion rates were determined by measuring a series of oscillations while increasing the cation cell temperature until the cation and anion fluxes were approximately equal as indicated by suppressed oscillations, metal-rich reconstructions, and/or transmission spots. GaAs oscillations were recorded during the GaAs buffer layer. AlSb oscillations were recorded during the AlSb buffer layer and used to estimate the Al cell temperature for 0.70 ML/s AlSb in the AlGaSb alloy. Oscillations of AlGaSb were also measured and confirmed growth rates near 1.0 ML/s. The In cell was calibrated separately by recording RHEED oscillations during InAs growth on an InAs substrate. RHEED reconstruction patterns are (2x4) during GaAs, (1x3) during AlSb and AlGaSb, and (1x1) with some evidence of (2x4) during the InAs channel. A (4x2) In-rich pattern is observed during the monolayer of In that follows the InAs channel. The RHEED pattern degrades during growth of the lattice-mismatched InAlAs barrier.

A second heterostructure that includes Si doping is also shown in Fig. 1 (sample B). The growth procedure described above was modified: growth was interrupted after the 50 Å AlSb barrier and the sample temperature was dropped to 400°C for the growth of the 12 Å InAs(Si) and 12 Å AlSb layers. This lower growth temperature is required to minimize segregation of Si into the AlSb.¹⁶ The growth was again interrupted and the temperature was increased to 450°C for the InAlAs and InAs cap layers.

High-resolution x-ray diffraction measurements were performed on a Bede D1 system using Cu-K_{α1} radiation with a four-bounce Si (220) monochromator. A Leighton system was used for contactless eddy-current resistivity mapping on whole wafers. Standard Hall/van der Pauw measurements were performed at 0.37 T on 5 x 5 mm² squares, usually taken from the center of the wafer.

III. RESULTS AND DISCUSSION

A high-resolution x-ray diffraction measurement of the (004) reflection for sample A is shown in Fig. 2a. A simulated structure based upon dynamical diffraction theory is also shown. The largest peaks are the GaAs substrate and AlSb buffer layer that is 99% relaxed and has a FWHM of 230". The Al_xGa_{1-x}Sb peak is also visible and has a FWHM of 270". Smaller peaks are visible in the simulation but not the experimental data, probably because of the high dislocation density in the AlSb buffer layer. Additional (115) asymmetric scans allowed us to determine the composition of this layer to be $x = 0.70 \pm 0.02$ with a lattice relaxation of $45 \pm 15\%$. The 150 Å InAs channel is clearly visible and has a FWHM of ~1200", compared to 1120" for the simulated structure. The small FWHM-experimental: FWHM-theoretical ratio^{17,18,19} and the position of the peak

confirm that the InAs is coherently strained to the AlGaSb. The peak at $-700''$ is probably due to In or Sb contamination in the GaAs buffer layer. Most of our samples do not exhibit this peak. Atomic force microscopy (AFM) of sample A yields an rms roughness of 18 \AA for a $5 \times 5 \text{ \mu m}^2$ area. This sample has a sheet carrier concentration of $2.8 \times 10^{12}/\text{cm}^2$ and a mobility of $19,000 \text{ cm}^2/\text{V-s}$ at 300K. We note that a high mobility is achieved despite the fact that the channel was grown on a partially relaxed layer.

Work on high-mobility InAs quantum wells is generally targeted to one of two goals. The first is producing structures for low-temperature physics research. In this case, the primary goal is usually high mobilities at low temperatures.²⁰ The second is high-frequency, low-power HEMTs operating at room temperature. In this application, the room-temperature mobility and carrier density need to be high (i.e. low sheet resistance). In some cases, growth requirements are similar. For example, if the lower InAs/AlSb interface has AlAs-like bonds, the mobility will be very low at all temperatures¹⁴, making the structures unsuitable for both applications. In other cases, however, the growth requirements are different. For example, the highest low-temperature mobilities ($>800,000 \text{ cm}^2/\text{V-s}$ at 4K) were achieved with thick buffer layers of GaSb.²¹ The room-temperature mobility is not substantially improved by the GaSb, and the presence of thick conductive GaSb layers is not desirable for HEMT applications. We will now discuss variations to the heterostructure and growth parameters discussed above, beginning with the substrate and working up to the cap layer. We will focus on suitability for HEMT applications.

There are currently no appropriate insulating substrates near 6.1 \AA . As a result, most work in our laboratories and others has been on semi-insulating GaAs substrates

(8% lattice mismatch). InP is also available in a semi-insulating form and should be suitable. The lattice mismatch is 4% which still necessitates the use of thick, relaxed buffer layers. (These structures on GaAs or InP could be referred to as metamorphic HEMTs.) We grew a HEMT structure on InP (sample C). The only differences from sample A are the absence of a GaAs buffer layer and an InAs cap layer. The transport results were very similar: $n_s = 2.9 \times 10^{12}/\text{cm}^2$ and $\mu = 18,700 \text{ cm}^2/\text{V}\cdot\text{s}$. The AFM rms roughness was 24 \AA , and the AlSb x-ray FWHM was $310''$. The possibility of transferred substrates for InAs HEMTs is also being explored in our laboratory and others.

As discussed above, we routinely initiate growth with GaAs. Although growing a GaAs buffer layer should provide a smoother starting surface for AlSb growth, three-dimensional growth during the initial AlSb deposition cannot be avoided due to the large lattice mismatch. On a number of occasions, we have omitted the GaAs layer and observed no effect on the room-temperature transport, x-ray, or AFM measurements. In most of our samples, the total thickness of the antimonide buffer layer(s) is $2.0\text{-}2.5 \mu\text{m}$. We observed no impact on room-temperature mobility when using thicknesses of $1.5 \mu\text{m}$. Thinner buffer layers may also be possible. For example, Kuze *et al.* achieved high-mobility undoped InAs quantum wells using $0.6 \mu\text{m}$ buffer layers of AlGaAsSb.²² We have obtained high-mobility quantum wells for AlSb growth temperatures ranging from 500 to 600°C ; we did not explore temperatures outside this range. We routinely grow the buffer layers near 1.0 ML/s ($1.1 \mu\text{m}/\text{hour}$). We have used growth rates as high as 2.0 ML/s with good results.²³ Another group also reported high growth rates for AlSb buffer layers.²⁴

Pure AlSb oxidizes very rapidly, making it unsuitable for layers that will be exposed during device fabrication. Adding Ga or In to the layer results in a drastic reduction of oxidation rates²⁵, similar to the case of AlGaAs. For this reason, we have explored the use of AlGaSb⁶ and InAlSb buffer and barrier layers. The 3000 Å layer of Al_{0.70}Ga_{0.30}Sb in our baseline structure (A) allows for a mesa isolation etch that stops in the AlGaSb and hence does not expose AlSb outside the active region. (Previously, a non-planar air bridge technology was employed to avoid oxidation of the AlSb.²⁷) We have also grown structures in which the entire 2.0 μm buffer layer is Al_{0.70}Ga_{0.30}Sb (grown at 510°C). For example, sample D has $n_s = 3.1 \times 10^{12}/\text{cm}^2$ and $\mu = 17,700 \text{ cm}^2/\text{V}\cdot\text{s}$. For sample E, $n_s = 2.2 \times 10^{12}/\text{cm}^2$ and $\mu = 22,100 \text{ cm}^2/\text{V}\cdot\text{s}$. Our initial attempts to use thick buffer layers of InAlSb, however, have not been successful. We varied the growth temperature of the buffer layer from 400 to 500°C but InAs quantum well mobilities were always low (<10,000 cm²/V-s at 300K).

Many of our heterostructures include a 100-200 Å layer of GaSb immediately above the buffer layer(s). It is doped with Si to yield $p \sim 6 \times 10^{17}/\text{cm}^3$. The function of this layer is to drain impact-ionization-generated holes back to the source contact.^{26,27} Beryllium might be a more logical dopant for this layer but we did not have a Be source when we first included this layer. Recently, we have doped this layer with Be and no problems were observed.

The channel thickness of our samples was either 150 Å (Fig. 1a) or 100 Å (Fig. 1b). The samples with 100 Å channels also have a 42 Å InAs sub-channel in most cases. The function of the sub-channel is to allow the transfer of energetic electrons which could otherwise result in impact ionization in the channel.⁷ Bolognesi *et al.* measured mobilities

as a function of InAs thickness for InAs/AlSb quantum wells.²⁸ They found the highest mobilities ($\sim 30,000 \text{ cm}^2/\text{V}\cdot\text{s}$ at 300K for undoped structures) for channel thicknesses of 125-200 Å. Even at 250 Å, however, the room-temperature mobility was still above $20,000 \text{ cm}^2/\text{V}\cdot\text{s}$, despite the 1.3% lattice mismatch. At 100 Å, the mobility dropped to 19,000. For HEMTs, it is desirable to scale down the vertical dimensions as well as the horizontal (lithographically-defined) dimensions. In one case, we achieved a mobility of 26,000 for a 100 Å channel (sample F). Mobilities of 20,000-22,000 are more typical for our structures with 100 Å channels, but the decrease in mobility may result from higher doping levels (see below) in addition to increased interface scattering associated with thin channels.

Our work suggests that the growth temperature window for high-mobility HEMT structures is relatively large. We normally aim for 490-510°C but have observed no reduction in room-temperature mobility for temperatures 10-20°C outside that range. Triplett *et al.* completed a more systematic study and found high mobilities for undoped quantum wells grown between 445 and 500°C.²⁴

As mentioned earlier, the lower interface between InAs and AlSb must be InSb-like to achieve high mobilities. We have also achieved good mobilities ($>20,000 \text{ cm}^2/\text{V}\cdot\text{s}$) and resistivities ($<150 \text{ } \Omega/\square$) using InSb-like bonds for InAs/AlGaSb and InAs/InAlSb quantum wells. Our nominal V:III flux ratios are 2.0:1 for both arsenide and antimonide layers. Although we have not conducted a systematic study, our experience is that this parameter is not critical, with an acceptable range of at least 1.5 to 3.0:1. In the past, we have used a conventional cell for Sb producing Sb₄ as well as unvalved and valved Sb crackers. High-performance HEMTs were fabricated from structures grown using each of

the three Sb sources. The use of a valved source may be more important for As because of substantial As leakage around the shutter in some MBE systems such as the Riber 21T used in this study.

Sheet carrier concentrations for unintentionally doped InAs/AlSb single quantum wells, a function of the upper barrier thickness and cap material (InAs or GaSb), are usually in the range $0.4\text{-}1.6 \times 10^{12}/\text{cm}^2$.²⁹ Higher sheet charge densities are typically desirable for HEMT applications. Silicon is the most common n-type dopant in III-V MBE systems. Silicon is, however, amphoteric in the III-V's, producing n-type GaAs, InAs, AlAs, and InSb, but p-type GaSb and AlSb on (100) surfaces.³⁰ Sasa *et al.* achieved sheet carrier concentrations in the $2\text{-}4 \times 10^{12}/\text{cm}^2$ range by Si planar doping in an 18 Å InAs quantum well located 80 Å below a 150 Å InAs quantum well clad by AlGaSb.³¹ This technique has been successfully applied to InAs HEMTs by at least three groups.^{16,32,33}

We have achieved the desired mobilities and carrier densities using both Si- and Te-doping. An advantage of Te doping is that no changes in growth temperature are required. In Fig. 3, we plot the mobility and density for two pairs of samples, one Si-doped (B and F) and one Te-doped (G and H). Within each pair, only the spacer layer thickness varies. As expected, the carrier density increases as the spacer thickness decreases. The mobility decreases with decreasing thickness. This could be due to an increase in remote carrier scattering. On a Te-doped sample with a 40 Å spacer and $2.2 \times 10^{12}/\text{cm}^2$ density, we obtained a mobility of 22,000 (sample E—not shown in Fig. 3). Hence, remote carrier scattering is probably not the primary reason for the decrease in mobility from 23,000 to 18,000 for the Te-doped samples in Fig. 3. Based upon

Shubnikov-de Haas measurements, electrons begin to populate a second sub-band in InAs quantum wells at densities of $2.0\text{-}2.4 \times 10^{12}/\text{cm}^2$.^{16,31} Hence, for higher densities we expect intersubband scattering and a reduction in mobility, as observed for both sets of samples in Fig. 3.

The final layers in the HEMT structures are the InAlAs barrier and InAs cap. The growth temperature for these layers is near 450°C for the Si-doped structures and 510°C for the Te-doped structures. Despite the large lattice mismatch and three-dimensional growth, the InAlAs layer does not appear to degrade the electron mobility, presumably because it is at least 75 \AA above the channel. We have replaced the InAs cap with 20 \AA GaAs and also eliminated it entirely with no significant impact on electron mobility and density.

All the epitaxial layers of sample B except the GaAs buffer are visible in the Z-contrast scanning transmission electron microscope (STEM) image of Fig. 4. The image was taken at a magnification of 350,000 after TiW/Au gate metallization. The layers appear to be uniform. Analysis of the image shows that the measured thicknesses are near the nominal values.

A sheet-resistance map for sample A is shown in Fig. 5. The resistance varies from 107 to $133 \ \Omega/\square$ across the wafer, with an average of $115 \ \Omega/\square$ and a standard deviation of $7.0 \ \Omega/\square$. The value in the center of the wafer, $115 \ \Omega/\square$, is in good agreement with a value of $117 \ \Omega/\square$ calculated from the Hall measurements. This value of uniformity is typical for our growths on 75 mm substrates in the 21T MBE. We have evidence from x-ray and optical measurements on superlattices that the layer thicknesses vary by only about 1% across the 75 mm wafers. Hence, we might expect our HEMT uniformities to be better

than sample A. The best uniformity we have obtained was sample I, also shown in Fig. 5, with $107.9 \pm 1.6 \text{ } \Omega/\square$. The structure was nominally the same as sample A. A typical sheet-resistance map from the 32P MBE (50-mm) is shown on the bottom of Fig. 5 (sample J), with $98.6 \pm 3.1 \text{ } \Omega/\square$. The sample was Si-doped but Te-doped samples have comparable uniformities. These uniformities are good considering that the layer thicknesses are known to vary by more than 10% across a 50 mm wafer in this MBE.

In Fig. 6, we plot the mobility versus carrier density for undoped, Si-doped, and Te-doped HEMT structures grown on both MBE systems. High mobility and low sheet resistance are desired for most HEMT applications. Although high mobilities are achieved for undoped structures, the densities are too low to achieve sheet resistances less than $200 \text{ } \Omega/\square$. Sheet resistances less than $100 \text{ } \Omega/\square$ have been reached for both Si- and Te-doping. Most doped samples are between 90 and $150 \text{ } \Omega/\square$. We find that densities near $3.0 \times 10^{12}/\text{cm}^2$ are optimal for achieving both high mobility and low sheet resistance.

For most samples, the x-ray diffraction data is similar to that for sample A (fig. 2a). The AlSb FWHM values are usually between 220 and $340''$.³⁴ The positions of the InAs peaks are near $-7300''$, consistent with InAs coherently strained to Al(Ga)Sb. One exception is sample K whose x-ray data is plotted in Fig. 2b. Note that the InAs peak is weak and shifted toward the AlSb. In addition, the AlGaSb peak is not well defined. In order to get reasonable agreement with the experimental data, an InAs relaxation of 85% was used for the simulation shown. This sample had a density of $3.0 \times 10^{12}/\text{cm}^2$ and a mobility of only $7400 \text{ cm}^2/\text{V-s}$ as shown in Fig. 6. Despite the poor mobility and relaxed InAs, the surface morphology for this sample was good, with an rms roughness of only $11 \text{ } \text{Å}$. For all of our “good” HEMT structures ($\mu > 18,000 \text{ cm}^2/\text{V-s}$), surface roughness

ranges from 8 to 26 Å with no apparent correlation between roughness and mobility. As mentioned earlier, thick buffer layers of InAlSb were investigated. For these low-mobility samples, the surfaces were relatively rough, with rms values greater than 35 Å; the InAs peaks were not well-defined in x-ray diffraction measurements. Based upon our experience, HEMT structures with good surface morphology (low rms roughness) and coherently-strained InAs also have high mobility. One could envision exceptions to this such as a sample with impurities in the InAs channel; in this case, the mobility would be low but the InAs could be coherent and the surface smooth.

IV. SUMMARY

The likelihood of a successful transition of InAs HEMTs from research involving discrete devices to production of circuits for commercial or military applications will depend, in part, on the ability of the epitaxial growth to meet several objectives. In this work, we have demonstrated that many of these objectives have been achieved. Specifically, heterostructures with high mobility ($\sim 20,000 \text{ cm}^2/\text{V}\cdot\text{s}$), high sheet density ($\sim 3 \times 10^{12}/\text{cm}^2$), and low resistivity ($\sim 100 \text{ }\Omega/\square$) have been routinely grown with good uniformity across a 75-mm GaAs substrate. Both Si and Te doping have been successfully used. An advantage of Te is that changes in substrate temperature are not required during growth of the active regions. The InAs channels are coherently strained to the Al(Ga)Sb buffer layers, and the surfaces of the as-grown structures are relatively smooth. The insertion of a layer of AlGaSb below the channel minimizes the exposure of pure AlSb during processing and the need for an air-bridge technology. As a result, a planar process can now be employed. Remaining challenges include the reduction of gate

leakage currents and microwave noise. Work in these areas is underway in our laboratories. The unique material properties, improvements in the material growth described here, and the recent demonstration of MMIC circuits^{11,35} demonstrate that InAs HEMTs are attractive candidates for future applications requiring high speed and low power.

ACKNOWLEDGEMENTS

The Defense Advanced Research Projects Agency (ABCS Program) and the Office of Naval Research supported this work. The authors thank W. Kruppa, R. Magno, N. Papanicolaou and B.V. Shanabrook for technical discussions and assistance.

Figure Captions

1. Cross-section for samples A (Te-doped) and B (Si-doped with a sub-channel and p⁺-GaSb layer) and calculated band structure for A.
2. High-resolution x-ray diffraction scans (dashed lines) of sample A ($\mu = 19,000$ cm²/V-s at 300K) and sample K ($\mu = 7400$ cm²/V-s at 300K). Simulations are also shown for both structures as solid lines. The intensity units are arbitrary for the simulated curves. The nominal values of layer thickness are used in the simulations. For sample A, the layer relaxation values in the simulation are 98.7%, 45%, and 0% for the AlSb, Al_{0.70}Ga_{0.30}Sb, and InAs, respectively. For sample K, the layer relaxation values in the simulation are 98.9%, 45%, and 85% for the same layers.
3. Sheet density and mobility versus AlSb spacer thickness for samples B and F (Si-doped) and samples G and H (Te-doped). Within each pair, only the spacer thickness varies.
4. STEM image (350,000x) of sample B after gate metallization.
5. Sheet-resistance map of samples A (typical 75-mm uniformity; Te-doped), I (best 75-mm uniformity; Te-doped), and J (typical 50 mm uniformity; Si-doped). Contours are in units of Ω/\square . The major flats are indicated. All samples were rotated during growth.
6. Room-temperature mobility versus density for thirty HEMT structures, including undoped, Te-doped and Si-doped samples. Coutours of constant sheet resistance are also shown.

References

- ¹ Z. Dobrovolskis, K. Grigoras, and A. Krotkus, *Appl. Phys. A* **48**, 245 (1989).
- ² L.F. Luo, R. Beresford, W.I. Wang, and H. Munekata, *Appl. Phys. Lett.* **55**, 789 (1989).
- ³ J. Werking, G. Tuttle, C. Nguyen, E.L. Hu, and H. Kroemer, *Appl. Phys. Lett.* **57**, 905 (1990).
- ⁴ K. Yoh, T. Moriuchi, and M. Inoue, *Japn. J. Appl. Phys.* **29**, L2445 (1990).
- ⁵ J.B. Boos, W. Kruppa, B.V. Shanabrook, D. Park, J.L. Davis, and H.B. Dietrich, *Electr. Lett.* **29**, 1888 (1993).
- ⁶ C.R. Bolognesi, E.J. Caine, and H. Kroemer, *IEEE Electr. Dev. Lett.* **15**, 16 (1994).
- ⁷ J.B. Boos, M.J. Yang, B.R. Bennett, D. Park, W. Kruppa, C.H. Yang, and R. Bass, *Electr. Lett.* **34**, 1525 (1998).
- ⁸ J. B. Boos, B. R. Bennett, W. Kruppa, D. Park, J. Mittereder, R. Bass, and M. E. Twigg, *J. Vac. Sci. Technol. B*, **17**, 1022 (1999).
- ⁹ J. Bergman, G. Nagy, G. Sullivan, B. Brar, C. Kadow, H.-K. Lin, A. Gossard, and M. Rodwell, *Proc. 15th Int'l. Conf. IPRM*, 219, 2003.
- ¹⁰ R. Tsai, M. Barsky, J. Lee, J. B. Boos, B. R. Bennett, R. Magno, C. Namba, P. H. Liu, A. Gutierrez, and R. Lai, *Proc. Eastman Conference*, 276 (2002).
- ¹¹ R. Tsai, M. Barsky, J. B. Boos, B. R. Bennett, J. Lee, N. A. Papanicolaou, R. Magno, C. Namba, P. H. Liu, D. Park, R. Grundbacher, and A. Gutierrez, *Proc. GaAs IC Conf.* (2003).
- ¹² B.V. Shanabrook, J.R. Waterman, J.L. Davis, and R.J. Wagner, *Appl. Phys. Lett.* **61**, 2338 (1992).
- ¹³ B.R. Bennett, R. Magno, and N. Papanicolaou, *J. Cryst. Growth* **251**, 532 (2003).

-
- ¹⁴ G. Tuttle, H. Kroemer, and J.H. English, *J. Appl. Phys.* **67**, 3032 (1990).
- ¹⁵ B.R. Bennett, B.V. Shanabrook, and E.R. Glaser, *Appl. Phys. Lett.* **65**, 598 (1994).
- ¹⁶ B.R. Bennett, M.J. Yang, B.V. Shanabrook, J.B. Boos, and D. Park, *Appl. Phys. Lett.* **72**, 1193 (1998).
- ¹⁷ C.R. Wie, *J. of Appl. Phys.* **65**, 2267 (1989).
- ¹⁸ B.R. Bennett and J.A. del Alamo, *J. of Appl. Phys.* **73**, 3195 (1993).
- ¹⁹ X.G. Zhang, P. Li, D.W. Parent, G. Zhao, J.E. Ayers, and F.C. Jain, *J. Electron. Mat.* **28**, 553 (1999).
- ²⁰ For example, S.J. Koester, C.R. Bolognesi, M. Thomas, E.L. Hu, H. Kroemer, and M.J. Rooks, *Phys. Rev. B* **50**, 5710 (1994) and C.H. Yang, M.J. Yang, K.A. Cheng, and J.C. Culbertson, *Phys. Rev. B* **66**, 115306 (2002).
- ²¹ C. Nguyen B. Brar, C.R. Bolognesi, J.J. Pekarik, H. Kroemer, and J.H. English *J. Electron. Mat.* **22**, 255 (1993).
- ²² N. Kuze, H. Goto, M. Matsui, I. Shibasaki, and H. Sakaki, *J. Cryst. Growth* **175/176**, 868 (1997)
- ²³ B.R. Bennett, W.J. Moore, M.J. Yang, and B.V. Shanabrook, *J. Appl. Phys.* **87**, 7876 (2000).
- ²⁴ G. Triplett, G. May, and A.S. Brown, *Solid-State Electr.* **46**, 1519 (2002).
- ²⁵ S. Miya, S. Muramatsu, N. Kuze, K. Nagase, T. Iwabuchi, A. Ichii, M. Ozaki, and I. Shibasaki, *J. Electron. Mat.* **25**, 415 (1996).
- ²⁶ B. Brar and H. Kroemer, *IEEE Electron Dev. Lett.* **16**, 548 (1995).
- ²⁷ J.B. Boos, W. Kruppa, B.R. Bennett, D. Park, S. Kirchoefer, R. Bass, and H.B. Dietrich, *IEEE Trans. Electron Devices* **45**, 1869 (1998).

-
- ²⁸ C.R. Bolognesi, H. Kroemer, and J.H. English, *J. Vac. Sci. Technol. B* **10**, 877 (1992).
- ²⁹ C. Nguyen, B. Brar, and H. Kroemer, *J. Vac. Sci. Technol. B* **11**, 1706 (1993).
- ³⁰ R. Venkatasubramanian, D.L. Dorsey, and K. Mahalingam, *J. Cryst. Growth* **175/176**, 224 (1997).
- ³¹ S. Sasa, Y. Yamamoto, S. Izumiya, M. Yano, Y. Iwai, and M. Inoue, *Jpn. J. Appl. Phys.* **36**, 1869 (1997).
- ³² Y. Zhao, M.J. Jurkovic, and W.I. Wang, *IEEE Trans. Electron Devices* **45**, 341 (1998).
- ³³ C.R. Bolognesi, M.W. Dvorak, and D.H. Chow, *IEEE Electron Dev. Lett.* **19**, 83 (1998).
- ³⁴ We note that the values of the FWHM for AlSb are a function of both the sample and the x-ray optics. For sample A, we obtained 410'' on a double-crystal system without slits, 340'' on the same system with a slit before the detector, 230'' on the Bede D1 system described in this paper, and 60'' on a system with a 4-bounce Ge (220) monochromator and a Ge (220) analyzer crystal between the detector and the sample. This latter measurement is primarily a reflection of changes in d-spacing whereas the other measurements are also influenced by the mosaic spread caused by dislocations.
- ³⁵ J. Bergman *et al.*, presented at the 53rd Device Research Conference (2003).

Sample List

A T030421J

B R011027F

C T030613K

D R020612G

E R020719F

F R011007F

G T030620K

H T030620J

I T030421K

J R021231H

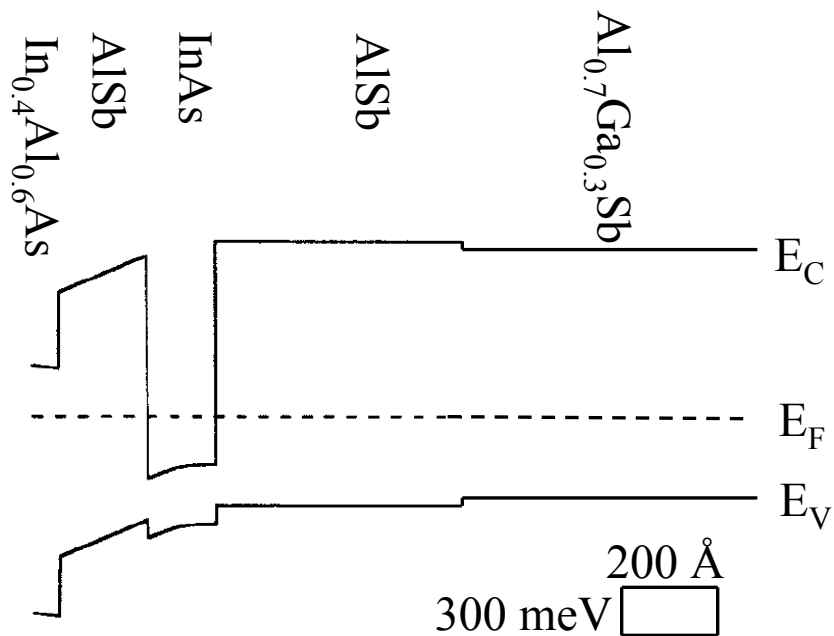
K R030210F

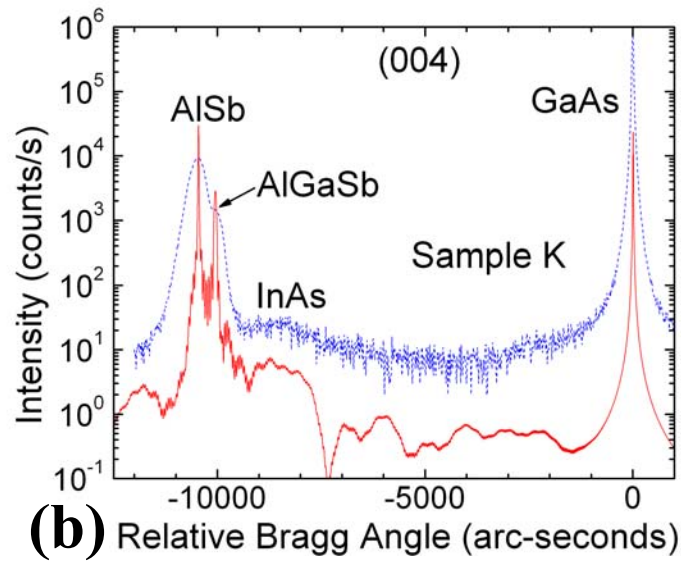
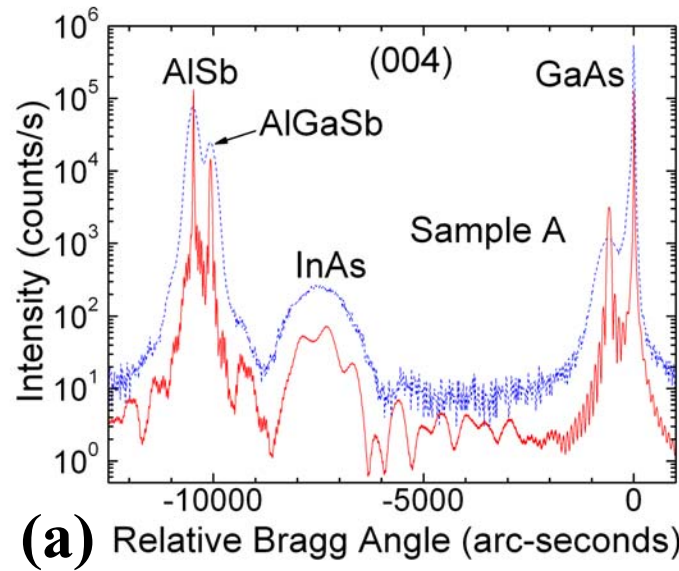
20 Å InAs
40 Å In _{0.4} Al _{0.6} As
50 Å AlSb
60 Å AlSb(Te)
75 Å AlSb
150 Å InAs
500 Å AlSb
3000 Å Al _{0.7} Ga _{0.3} Sb
1.7 μm AlSb
2000 Å GaAs
SI GaAs (100)

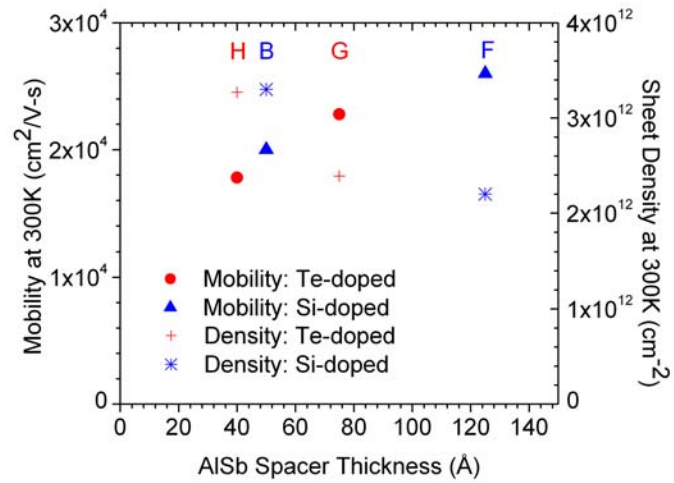
A

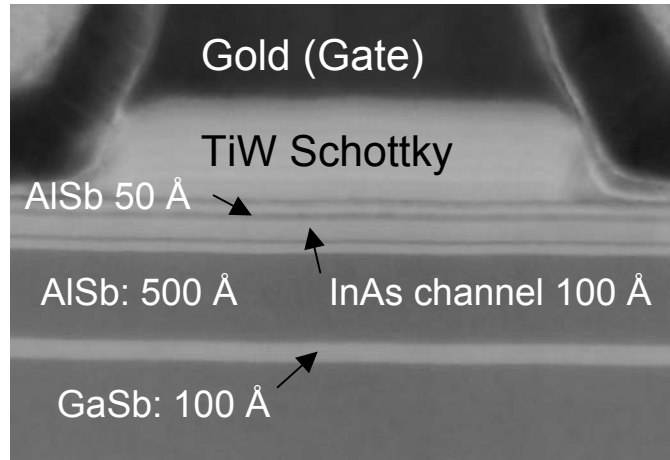
20 Å InAs
40 Å In _{0.4} Al _{0.6} As
12 Å AlSb
12 Å InAs(Si)
50 Å AlSb
100 Å InAs
30 Å AlSb
42 Å InAs
500 Å AlSb
100 Å GaSb(Si)
2.4 μm AlSb
900 Å GaAs
SI GaAs (100)

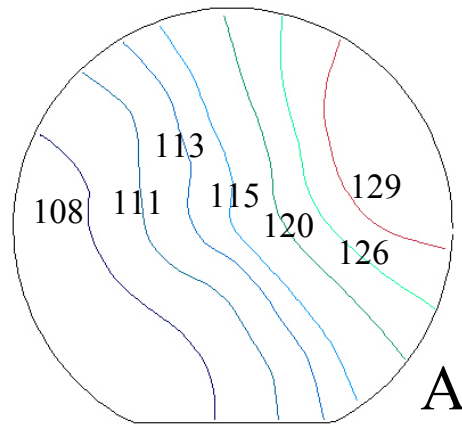
B



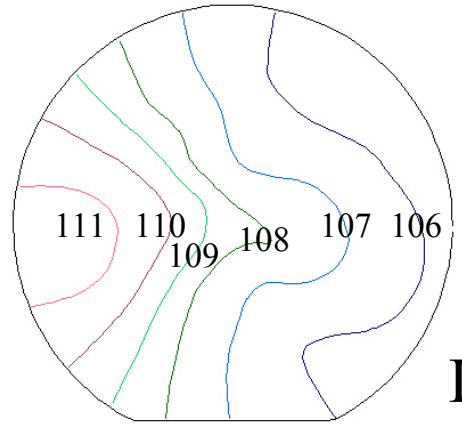




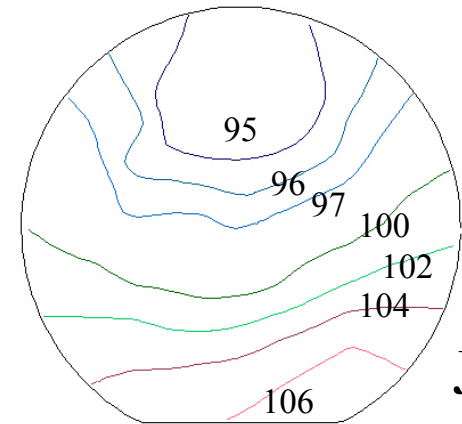




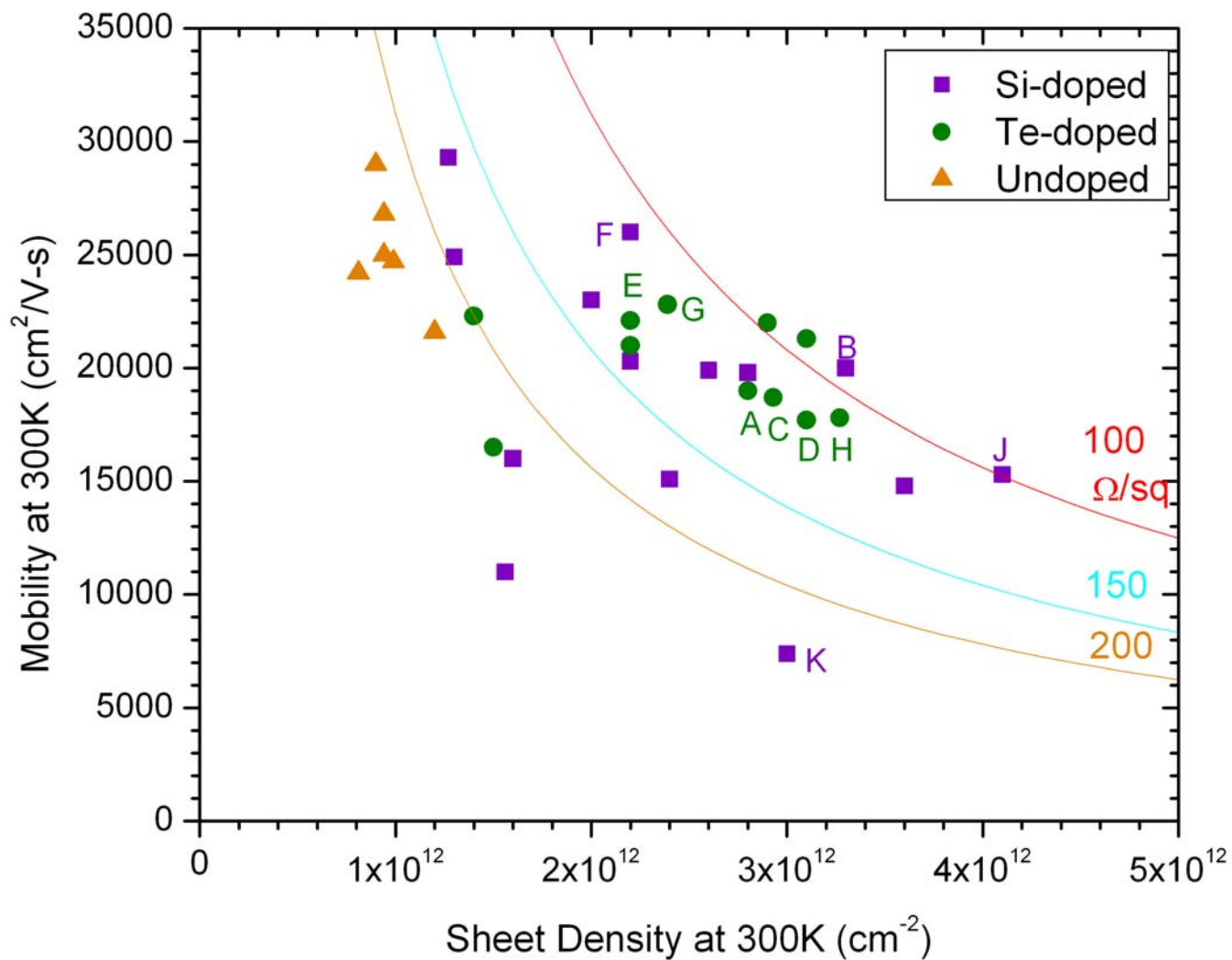
A



I



J



Bennett *et al.*
JVSTB

Fig. 6 of 6

Two-Column Format